Sensor Applications

Ground Penetrating Radar Signal Characterization for Non-destructive Evaluation of Low-range Concrete Sub-surface Boundary Conditions

Nathan Rees, Karthick Thiyagarajan*, Sathira Wickramanayake, and Sarath Kodagoda*
iPipes Lab, UTS Robotics Institute, University of Technology Sydney, Sydney, New South Wales, 2007, Australia.
* *Member, IEEE*

Manuscript received January X, 2022; revised XXX XX, 2022; accepted XXXX, 2022. Date of publication XX xxx, 2022; date of current version XX, 2022.

Abstract—The use of non-destructive sensing technologies is critical in the evaluation of concrete conditions and structural integrity. In our previous experimental studies, we showed the use of ground penetrating radar (GPR) based non-destructive evaluation method to examine low-range concrete sub-surface boundary conditions. As the characterization of GPR signals based on multiple factors is crucial for furthering the accurate conditions of concrete sub-surfaces, we investigate the GPR signals in this study by simulating electromagnetic wave propagation on concrete models through the use of the finite domain time difference method. The effects of concrete relative permittivity, the standoff distance of GPR from the top surface of concrete, the operating frequency of GPR, and the depth height of multi-layered concrete on the GPR measurements were all investigated and conclusions were established. Through the outcomes of this investigation, we will be able to choose the most appropriate operating frequency for the GPR for collecting measurements on concrete infrastructures at the most effective standoff distance to the surface and sub-surface depths under a variety of relative permittivity conditions in various locations.

Index Terms—Automation in construction, Concrete pipe corrosion, Ground penetrating radar, Infrastructure robotics, Infrastructure sensing, Non-destructive Evaluation, Sensor characterization, Smart sensing, Structural health monitoring, Wastewater pipe inspections.

I. INTRODUCTION

Wastewater pipelines carry effluent from residential and industrial locations to treatment plants. Those are generally made out of concrete, and as pipelines age, microbial corrosion occurs [1] causing billions of dollars in losses for water utilities worldwide. Therefore, the use of reliable sensing technology for non-destructive evaluation (NDE) of critical wastewater pipe infrastructure assets is vital. Timely inspections aid in the prevention of structural failures and in making informed decisions about repairs and rehabilitation.

The most common method for assessing the condition of a wastewater pipe involves destructive procedures to obtain core samples [2]. The obtained core samples are transported to laboratories for further evaluation, particularly by slicing and pH testing. Our team previously developed a unique sensing method that employs drill-resistance to correctly assess the depth of damaged concrete [3]. With a smaller footprint, it is more effective than core sampling, but it is also considered destructive. Researchers have also developed a sensor-driven predictive analytics toolkit that uses wastewater pipe environment variables to estimate corrosion hot spots [4]–[7]. However, unfavorable environmental conditions can cause the failure of sensors that provide real-time data inputs to the prediction model [8]. The use of electrical resistivity measurements with machine learning to detect corrosion depth has also been investigated [9], [10]. However, they require further laboratory investigations and validations to establish their robustness. Concrete electrical resistivity tests are further impacted by factors including electrode spacing, aggregates and reinforcing bars in the concrete sub-surface, and moisture in the concrete. In practice, this technique is best used for spot measurements and must always be in contact with the concrete surface. Pulsed Eddy current sensors [11], [12] are widely employed as corrosion monitoring sensors. In concrete pipes, they can only measure the distance between rebars and the exposed surface. NDE based in-pipe robots have also been developed for analysing pipeline interior defects [13]. These technologies are generally camera based, and therefore, they are limited to assessing surface deterioration and not sub-surface corrosion. Microwave and millimetre wave-based sensing technologies are extensively employed in the construction industry for the assessment of building structures [14], [15]. However, there has been no study reported on their usefulness for estimating the concrete wastewater pipe sub-surface conditions. Although each of the sensing methods reviewed has its own set of merits, our focus is particularly on developing a NDE technology that can take continuous and reliable sub-surface concrete pipe corrosion measurements.

In our earlier study, we demonstrated the use of Ground Penetrating Radar (GPR) in analysing low-range concrete sub-surface boundary conditions [16]. In a real-world environment, the corroded layer is soft, irregular, and can be mushy, which presents difficulties in robotic sensing applications where the GPR antenna comes into direct contact with the surface. Furthermore, the floating robot moves erratically due to disturbances in the wastewater flow. Hence, during inspections, it is non-trivial to maintain the GPR antenna at a constant distance from the measuring surface. In this context, further study of the GPR signal characteristics can shed light on developing better technologies, and hence, this work focuses on the characterization of the GPR signal for NDE of low-range concrete sub-surface boundary conditions. The main contributions of the paper are a comprehensive study of the GPR sensor characterization based on a FDTD simulation, which leads to the establishment of the signal reflections from the boundaries of low permittivity materials, establishing the effects of permittivity and antenna standoff distance to the measuring surface on the signal peak-to-peak attribute and the effect of the depth of the top layer.

Corresponding author: Karthick Thiyagarajan (e-mail: Karthick.Thiyagarajan@uts.edu.au).

Associate Editor: XXXXXXXXXX.
Digital Object Identifier 10.1109/LSENS.2017.0000000

II. METHODOLOGY

A. GPR Operating Principle

GPR works by transmitting short electromagnetic pulses of a specific frequency into a material and measuring the returned pulses. Because electromagnetic waves travel through materials at a rate dictated by their relative permittivity, some energy is transmitted while others are reflected at discontinuities in the electromagnetic properties [17]. Discontinuities may be caused by debonding, material layers, or sub-surface objects. The attenuation of the signal and the magnitude of the received pulse depend on the medium's magnetic permeability and electrical conductivity. Materials with higher magnetic permeability and electrical conductivity enhance signal attenuation, resulting in lower received pulse amplitudes [18]. It is common to see electromagnetic pulse reflections in the time domain in the form of an amplitude scan (A-Scan), which is similar to the graph illustrated in Fig. 2(a), collected by a receiving antenna and observed in the time domain. The amplitudes of the received pulses are shown in an A-scan graph of a GPR scan with regard to the time at which the pulse is received. If the propagation velocity of electromagnetic waves in the given medium is known, the depth of the discontinuity of the material that generated this reflection may be determined using the time at which the reflected pulse occurred. The propagation velocity of a material is expressed as $v = \frac{c}{\epsilon_r}$, where c is the speed of sound in a vacuum and ϵ_r is the relative permittivty.

B. Electromagnetic Simulations

In this work, we simulate electromagnetic wave propagation using the open-source gprMax software package [19]. Due to the computer's storage and processing restrictions, gprMax uses the FDTD approach to solve Maxwell's equations by discretising the space and time continuous variables [20]. The simulated outcomes for the two models in this research are in two dimensions, defined by the spatial discretisation of one dimension in the z-direction. This reduces Maxwell's equations down to three coupled partial differential equations: (1), (2), and (3). These equations explain the relationship between the electric field strength E, magnetic field strength H, current density J, magnetisation M, electrical conductivity σ, magnetic permeability μ, electric permittivity ϵ, and time t.

$$\frac{\delta E_z}{\delta t} = \frac{1}{\epsilon}\left(\frac{\delta H_y}{\delta x} - \frac{\delta H_x}{\delta y} - J_{S_z} - \sigma E_z\right) \tag{1}$$

$$\frac{\delta H_x}{\delta t} = \frac{1}{\mu}\left(-\frac{\delta E_z}{\delta y} - M_{S_x} - \sigma^* H_x\right) \tag{2}$$

$$\frac{\delta H_y}{\delta t} = \frac{1}{\mu}\left(\frac{\delta E_z}{\delta x} - M_{S_y} - \sigma^* H_y\right) \tag{3}$$

The FDTD method uses these equations to iteratively compute the solution in the time domain. The electromagnetic fields propagate after each iteration, corresponding to a simulated time of Δt. Therefore, the time window of the entire simulation can be determined by setting the number of iterations [20]. The stability condition presented in equation (4) (where c is the speed of light) is based on the requirement that the model must be stable for a Fourier mode propagating in the FDTD lattice [21]. FDTD is a conditionally stable numerical process, so the spatial and time discretisation values Δx, Δy, Δz and Δt cannot be assigned independently [22]. For the 2D case, this equation is modified by letting $\Delta z \to \infty$ [20].

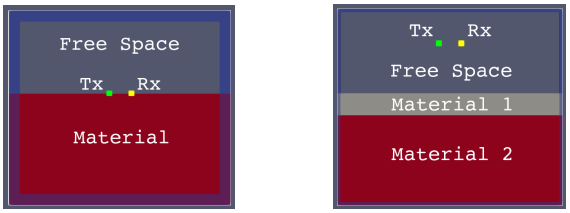

(a) (b)

Fig. 1: Simulation models. (a) Model 1, and (b) Model 2.

$$\Delta t \leq \frac{1}{c\sqrt{\frac{1}{(\Delta x)^2} + \frac{1}{(\Delta y)^2} + \frac{1}{(\Delta z)^2}}} \tag{4}$$

In this study, we simulated two models, Model 1 and Model 2. The parameters for both testing models were set, and the commands were programmed to create different input files for each test. The electromagnetic simulation model then generates output files with the simulated data. The domain parameter is adjusted to comfortably fit all components within the indicated sizes for both models. The simulation time period for all experiments is set to 3 ns to guarantee that the full spectrum of reflected signals is received and analysed. Model 1 required 27 tests, while Model 2 required 144 tests to simulate all potential parameter combinations. Each test also has 50 traces to account for the antennas' vertical movement. Figure 1(a) shows Model 1, which is made out of a single piece of material with a width of 400 mm and a height of 200 mm. The transmitting and receiving antennas, separated by 40 mm horizontally, are positioned in the model's centre. Initially, the transmitting and receiving antennas are placed at the material-free space boundary. The standoff distance is the distance between the GPR antenna and the top surface of the material, which is increased from 0 mm to 100 mm, in 2 mm intervals. In this work, we have chosen the range of ϵ_r to be from 4 to 12, with increments of one. The operating frequencies of the GPR transmitted signal is 1 GHz, 2 GHz, 4 GHz, and 6 GHz. Figure 1(b) shows Model 2, which consists of two materials; the first material lies between free space and the second material to simulate a corrosion condition in a pipe. The ϵ_r varies for the first material, but remains constant at $\epsilon_r = 6$ for the second material. The transmitting and receiving antennas are identically positioned to the setup in the Model 1. Also, similar to Model 1, the standoff distance of the GPR antennas above the surface of the material for Model 2 increases from 0 mm to 100 mm, in 2 mm intervals, and the operating frequency is set to 1 GHz, 2 GHz, 4 GHz, and 6 GHz. The vertical depth (d) of the first material increases from 5 mm to 40 mm, in 5 mm intervals. The ϵ_r of the second material is set at 7, 8, 9, 10, 11, and 12. The ϵ_r values of Model 1 and the top layer of Model 2 were chosen to reflect the ϵ_r of the concrete, which typically changes from 4 (dry concrete) to 12 (fully saturated concrete) [23], where the fully saturated condition after reasonable curing can be regarded due to acid permeation in concrete pipe walls. The GPR antenna's standoff distance from the top surface was set between 0 mm and 100 mm to account for wastewater flow while the floating robot collects data within concrete pipes. Since most reinforcing bars with a diameter of 10 mm are within 50 mm of the top surface of concrete pipes, the vertical depth of the Model 2 (first material) was selected from 5 mm to 40 mm. Thus, monitoring ϵ_r within that range is crucial for condition assessments.

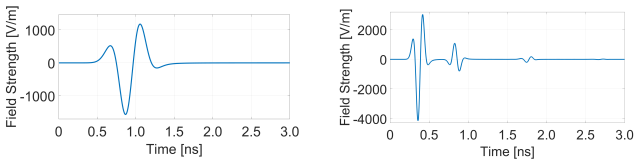

(a) (b)

Fig. 2: GPR A-scans. (a) Model 1, and (b) Model 2.

III. RESULTS

A. Analysis of GPR A-scans

All of the simulation output files were gathered and imported into MATLAB R2021b for additional processing. Those files include the A-scan data for each trace, which shows the received signal strength as a function of time. Plots of these A-scans were generated to provide visual evidence of how the signal behaved based on each set of parameters. Figure 2(a) shows the A-scan of Model 1, and Model 2's A-scan is shown in Fig. 2(b). Firstly, all A-scan plots show the unencumbered signal received from the transmitter as the strongest wave. Depending on the frequency, this signal is initially detected within 0.5 ns of transmission. The A-scan plots from both models then display a second, weaker wavelet shortly after the first. This is indicative of the signal reflecting off the boundary between the material and free space and subsequently being received with the opposite polarity. It should be noted that traces with an antenna standoff distance of 0 mm, such as in Fig. 2a, will not feature this second wavelet because the antennas lie on the aforementioned boundary. Finally, due to the dissimilar ϵ_r of the two materials, A-scan plots from Model 2, such as the one depicted in Fig. 2b, exhibit an additional waveform as a result of the signal reflecting off the boundary between the two materials. This wavelet will be even weaker than the previous signals as it has further to travel and more time to dissipate before reaching the receiving antenna.

B. Characterization

Figure 3(a) presents the peak-to-peak amplitudes for Tests 1-9 of the Model 1. While the plotted results for each test evidently share a very similar function shape, there is some visible distinction across the curves. These tests all have a frequency of 2 GHz, and the only changing parameter is the ϵ_r, hence the variations in results must be associated with this parameter. The plot also demonstrates that a higher value of ϵ_r produces a larger range of results, while tests with a lower ϵ_r bear less fluctuation in peak-to-peak amplitude. Given that the time taken for a transmitted signal to travel through a material, bounce off a feature, and be received will depend on the ϵ_r of the material [18], greater fluctuation may prove useful for an application attempting to estimate a material's ϵ_r when all other parameters are established, as results are more easily differentiable.

The separation between tests in Fig. 3(a) is greatest as the antennas shift from 0 mm to 10 mm above the material. The curves then begin to converge, intersecting when the antennas are at a standoff distance of approximately 22 mm. This indicates that the peak-to-peak amplitude for these 2 GHz tests will be practically indistinguishable when the antennas are at this standoff distance, regardless of the ϵ_r. It may be crucial to have knowledge of this characteristic when analyzing GPR tests, as results matching this criteria may be inaccurate. Selecting

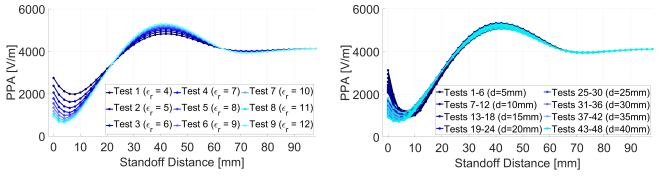

(a) (b)

Fig. 3: Effects of GPR antenna standoff distance above the top surface and relative permittivity on the peak-to-peak amplitudes (PPA) for 2 GHz GPR measurements. (a) Model 1, and (b) Model 2.

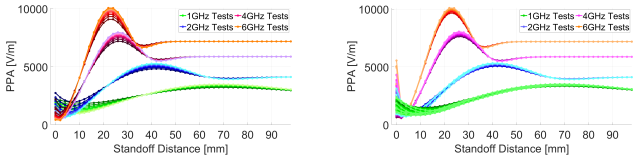

(a) (b)

Fig. 4: Effects of GPR antenna standoff distance above the top surface and varying operating frequencies of the GPR antenna on the peak-to-peak amplitudes (PPA) of the GPR measurements. (a) Model 1, and (b) Model 2.

the correct antenna standoff distance for a certain GPR application may be vital to obtaining the desired results.

The peak-to-peak amplitudes for the 2 GHz tests of the Model 2 are presented in Fig. 3(b). This model introduces an extra material with varying ϵ_r, and results in the plot are grouped into different colour shades based on the depth of Material 1, as annotated in Fig. 1b. The extent of the separation between each of the curves is visibly less prominent in comparison with the 2 GHz tests of the Model 1 in Fig. 3(a). For each group of six tests that share the same depth value, their results demonstrate less variance despite the fluctuating ϵ_r value of Material 2. This is because the depths tested are small enough to allow the transmitted signals to reach the boundary between Materials 1 and 2, reflect, and be received without having been significantly weakened by the first material's ϵ_r.

C. Effects of GPR Operating Frequency

The effect of the frequency on the received signals can be easily identified when examining the plot in Fig. 4(a), where the tests with a 6 GHz frequency clearly have a larger range of peak-to-peak amplitudes and a greater maximum peak-to-peak amplitude in comparison with the 4 GHz, 2 GHz and 1 GHz tests. Moreover, tests with the higher frequency attain their maximum value when the antennas are closer to the material. 6 GHz tests reach their maximum when the antennas are at a standoff distance of 22 mm, while 4 GHz tests reach this mark at 26 mm, 2 GHz tests at 42 mm, and 1 GHz tests at 68 mm. Lastly, peak-to-peak amplitudes for 6 GHz tests stop fluctuating and remain constant at roughly 7200 V/m. This value is significantly higher than 4 GHz tests, which settle at roughly 5900 V/m, 2 GHz tests at 4100 V/m, and 1 GHz tests at 3000 V/m. All of these features of the outcomes are closely related to the signal's frequency, which impacts its speed and wavelength.

An additional detail of the four data sets shown in Fig. 4(a) is the difference in separation between the curves. All tests exhibit a distinct separation as they reach their respective maximum values.

The range of peak-to-peak amplitude values at these points in Model 1 are 983 for 6 GHz tests, 766 for 4 GHz tests, 459 for 2 GHz tests, and 266 for 1 GHz tests. The characteristics of the results also differ within the first 10 mm of the antennas moving above the material. Both 1 GHz and 2 GHz tests display the greatest separation within this domain, however, there is considerably less separation for the 4 GHz and 6 GHz tests in the same region. Both these observations represent the decreased effect of ϵ_r on the results as the frequency increases. Furthermore, in comparison with the 1 GHz and 2 GHz tests, the 4 GHz and 6 GHz tests deliver results with increased fluctuations due to the change in frequency.

Examining all tests from Model 2 in Fig. 4(b) reveals very similar results in comparison with Fig. 4(a). As with the analysis of the 1 GHz and 2 GHz results, there is less variation between tests across all four frequency values. The most noticeable change occurs within the first 5 mm of the antennas moving above the material. The fluctuation of peak-to-peak amplitudes between traces is significantly greater, with the magnitude increasing as the frequency does. Increased separation between results in this region means the ϵ_r and depth parameters for Material 1 are more easily distinguishable. Given this attribute, estimating one of these parameters will be easier when the others are known.

IV. CONCLUSION AND FUTURE WORK

This work presents the GPR signal characterization through the FDTD simulation studies for NDE of low-range concrete sub-surface boundary conditions. The key outcomes of this work are: (a) The A-scans demonstrate no reflected signals from the homogeneous concrete layer when the GPR antennas are in contact with the top surface. When the concrete has multiple layers of ϵ_r, the A-scan shows an additional waveform due to the signal reflecting off the boundary between the two materials. (b) Material's ϵ_r affects the peak-to-peak amplitude of a GPR signal at the material-air interface. A lower ϵ_r value means a smaller peak-to-peak amplitude variance for that test. (c) The peak-to-peak amplitude variance of a signal increases as the standoff distance of the GPR antennas approaches the top surface. Signals will be easier to distinguish in terms of ϵ_r when the antennas are closest to the material's surface. This typically occurs within 4 mm of the surface. (d) The amplitudes of received signals will fluctuate as the top concrete layer depth lowers. Consequently, the ϵ_r of this material may be more easily distinguishable as its depth becomes shallower. (e) When the antennas are in contact with a concrete layer, increasing the GPR signal frequency causes a significant rise in the peak-to-peak amplitude variation of the received signals. By increasing the frequency, the ϵ_r has less effect on received signals. A lower GPR frequency will likely result in more distinct ϵ_r signals when analysed. Further, GPR signal attribute analyses will be carried out in the lab using concrete materials following this study. Also, deep learning algorithm in [24] will be utilized for real-world NDE.

REFERENCES

[1] A. P. Joseph, J. Keller, H. Bustamante, and P. L. Bond, "Surface neutralization and h2s oxidation at early stages of sewer corrosion: Influence of temperature, relative humidity and h2s concentration," *Water Research*, vol. 46, no. 13, pp. 4235–4245, Sep. 2012.

[2] S. Taheri, M. Ams, H. Bustamante, L. Vorreiter, M. Withford, and S. M. Clark, "A practical methodology to assess corrosion in concrete sewer pipes," *MATEC Web of Conferences*, vol. 199, no. 06010, p. 4, 2018.

[3] N. Giovanangeli, L. Piyathilaka, S. Kodagoda, K. Thiyagarajan, S. Barclay, and D. Vitanage, "Design and development of drill-resistance sensor technology for accurately measuring microbiologically corroded concrete depths," in *ISARC*. International Association for Automation and Robotics in Construction (IAARC), May 2019, pp. 735–742.

[4] K. Thiyagarajan, S. Kodagoda, R. Ranasinghe, D. Vitanage, and G. Iori, "Robust sensing suite for measuring temporal dynamics of surface temperature in sewers," *Scientific Reports*, vol. 8, no. 1, Oct. 2018.

[5] B. Rente, M. Fabian, M. Vidakovic, L. Vorreiter, H. Bustamante, T. Sun, and K. T. V. Grattan, "Extended study of fiber optic-based humidity sensing system performance for sewer network condition monitoring," *IEEE Sensors Journal*, vol. 21, no. 6, pp. 7665–7671, Mar. 2021.

[6] K. Thiyagarajan, S. Kodagoda, R. Ranasinghe, D. Vitanage, and G. Iori, "Robust sensor suite combined with predictive analytics enabled anomaly detection model for smart monitoring of concrete sewer pipe surface moisture conditions," *IEEE Sensors Journal*, vol. 20, no. 15, pp. 8232–8243, Aug. 2020.

[7] K. Thiyagarajan, S. Kodagoda, N. Ulapane, and M. Prasad, "A temporal forecasting driven approach using facebook's prophet method for anomaly detection in sewer air temperature sensor system," in *2020 15th IEEE Conference on Industrial Electronics and Applications (ICIEA)*. IEEE, Nov. 2020, pp. 25–30.

[8] K. Thiyagarajan, S. Kodagoda, L. V. Nguyen, and R. Ranasinghe, "Sensor failure detection and faulty data accommodation approach for instrumented wastewater infrastructures," *IEEE Access*, vol. 6, pp. 56 562–56 574, 2018.

[9] K. Thiyagarajan, P. Acharya, L. Piyathilaka, and S. Kodagoda, "Numerical modeling of the effects of electrode spacing and multilayered concrete resistivity on the apparent resistivity measured using wenner method," in *2020 15th IEEE Conference on Industrial Electronics and Applications (ICIEA)*. IEEE, Nov. 2020, pp. 200–206.

[10] K. Thiyagarajan, S. Kodagoda, L. V. Nguyen, and S. Wickramanayake, "Gaussian markov random fields for localizing reinforcing bars in concrete infrastructure," in *Proceedings of the 35th International Symposium on Automation and Robotics in Construction (ISARC)*. International Association for Automation and Robotics in Construction (IAARC), Jul. 2018, pp. 1052–1058.

[11] D. Tamhane, J. Patil, S. Banerjee, and S. Tallur, "Feature engineering of time-domain signals based on principal component analysis for rebar corrosion assessment using pulse eddy current," *IEEE Sensors Journal*, vol. 21, no. 19, pp. 22 086–22 093, 2021.

[12] N. Ulapane, K. Thiyagarajan, J. V. Miro, and S. Kodagoda, "Surface representation of pulsed eddy current sensor signals for improved ferromagnetic material thickness quantification," *IEEE Sensors Journal*, vol. 21, no. 4, pp. 5413–5422, Feb. 2021.

[13] A. Gunatilake, L. Piyathilaka, A. Tran, V. K. Vishwanathan, K. Thiyagarajan, and S. Kodagoda, "Stereo vision combined with laser profiling for mapping of pipeline internal defects," *IEEE Sensors Journal*, vol. 21, no. 10, pp. 11 926–11 934, May 2021.

[14] S. Kharkovsky and R. Zoughi, "Microwave and millimeter wave nondestructive testing and evaluation - overview and recent advances," *IEEE Instrumentation Measurement Magazine*, vol. 10, no. 2, pp. 26–38, 2007.

[15] P. Giri and S. Kharkovsky, "Dual-laser integrated microwave imaging system for nondestructive testing of construction materials and structures," *IEEE Transactions on Instrumentation and Measurement*, vol. 67, no. 6, pp. 1329–1337, 2018.

[16] N. Ulapane, L. Piyathilaka, and S. Kodagoda, "Some convolution and scale transformation techniques to enhance gpr images," in *2019 14th IEEE Conference on Industrial Electronics and Applications (ICIEA)*. IEEE, Jun. 2019, pp. 1453–1458.

[17] J. Daniels, "Ground penetrating radar fundamentals," sep 2008.

[18] G. S. Baker, T. E. Jordan, and J. Pardy, "An introduction to ground penetrating radar (GPR)," in *Special Paper 432: Stratigraphic Analyses Using GPR*. Geological Society of America, 2007, pp. 1–18.

[19] C. Warren, A. Giannopoulos, and I. Giannakis, "gprMax: Open source software to simulate electromagnetic wave propagation for ground penetrating radar," *Computer Physics Communications*, vol. 209, pp. 163–170, Dec. 2016.

[20] A. Giannopoulos and N. Diamanti, "A numerical investigation into the accuracy of determining dielectric properties and thicknesses of pavement layers using reflection amplitude gpr data," in *Proceedings of the Tenth International Conference on Grounds Penetrating Radar*. IEEE, Jun. 2004, pp. 655 – 658.

[21] A. Giannopoulos, "The investigation of transmission-line matrix and finite-difference time-domain methods for the forward problem of ground probing radar," pp. 55–184, 03 1997.

[22] ——, "Modelling ground penetrating radar by GprMax," *Construction and Building Materials*, vol. 19, no. 10, pp. 755–762, Dec. 2005.

[23] A. Ogunsola, U. Reggiani, and L. Sandrolini, "Shielding effectiveness of concrete buildings," in *IEEE 6th International Symposium on Electromagnetic Compatibility and Electromagnetic Ecology, 2005.*, 2005, pp. 65–68.

[24] S. Wickramanayake Mudalige Don, K. Thiyagarajan, and S. Kodagoda, "Deep learning for estimating low-range concrete sub-surface boundary depths using ground penetrating radar signals," *IEEE Sensors Letters*, pp. 1–1, 2022.